Scientific Reports

https://doi.org/10.1038/s41598-026-42087-w

Article in Press

Atomistic and electronic insights into Ca^{2+} and Li^{+} intercalation in TiS_2: a first-principles approach supported by electrochemical validation

Received: 17 December 2025

Accepted: 24 February 2026

Published online: 23 March 2026

Cite this article as: Yang S., Lee S., Nogales P.M. *et al.* Atomistic and electronic insights into Ca^{2+} and Li^{+} intercalation in TiS_2: a first-principles approach supported by electrochemical validation. *Sci Rep* (2026). https://doi.org/10.1038/s41598-026-42087-w

Seunga Yang, Sangyup Lee, Paul Maldonado Nogales, Yangsoo Kim & Soon-Ki Jeong

Atomistic and Electronic Insights into Ca^{2+} and Li^{+} Intercalation in TiS_2: A First-Principles Approach Supported by Electrochemical Validation

Seunga Yang[1], SangYup Lee[1], Paul Maldonado Nogales[1], Yangsoo Kim[2], and Soon-Ki Jeong[1,3,4]

[1]Department of Future Convergence Technology, Graduate School, Soonchunhyang University, Soonchunhyang-ro 22-gil, Sinchang-myeon, Asan-si 31538, Chungcheongnam-do, Republic of Korea

[2]Korea Basic Science Institute, Jeonju Center, Jeonju-si, Jeollabuk-do 54907, Republic of Korea

[3]Department of Energy Engineering, Soonchunhyang University, Soonchunhyang-ro 22-gil, Sinchang-myeon, Asan-si 31538, Chungcheongnam-do, Republic of Korea

[4]Advanced Energy Research Center, Soonchunhyang University, Soonchunhyang-ro 22-gil, Sinchang-myeon, Asan-si 31538, Chungcheongnam-do, Republic of Korea

Corresponding author: Soon-Ki Jeong, Department of Future Convergence Technology, Graduate School, Soonchunhyang University, Soonchunhyang-ro 22-gil, Sinchang-myeon, Asan-si 31538, Chungcheongnam-do, Republic of Korea

Tel.: +82-10-31314795, **Fax**: +82-41-5301313, **E-mail:** hamin611@sch.ac.kr

Yangsoo Kim, Korea Basic Science Institute, Jeonju Center, Jeonju-si, Jeollabuk-do 54907,

Republic of Korea

Tel.: +82-10-96968776, **Fax**: +86-20-81862664, **E-mail:** kimyangsoo@kbsi.re.kr

Acknowledgments

This work was supported by the Korea Institute of Energy Technology Evaluation and Planning (KETEP) and the Ministry of Trade, Industry & Energy (MOTIE) of the Republic of Korea (No. RS-2024-00394769). This research was supported by the Basic Science Research Program through the National Research Foundation of Korea (NRF) funded by the Ministry of Education (NRF-2021R1I1A3060329). This study was supported by the Soonchunhyang University Research Fund.

Abstract

Calcium-ion batteries are emerging as a sustainable and high-energy alternative to lithium systems, yet the atomic-scale origin of their ion–host interactions remains unclear. We clarified the coupling between ion mobility and electronic structure in titanium disulfide (TiS_2) by combining multiscale density functional theory with experimental analysis. Periodic VASP simulations and localized DV-Xα analyses revealed that Ca^{2+} intercalation induces greater lattice expansion than Li^+, lowers diffusion barriers, and enriches the density of states near the Fermi level, enhancing both ionic and electronic transport. Despite weaker Ca–S interactions, strong Ti–S covalency stabilizes the framework, yielding a theoretical open-circuit voltage of 1.383 V, which is lower than that of $LiTiS_2$ (1.948 V). Orbital overlap and charge-transfer analyses show that this lower voltage reflects a balance between multi-electron charge storage ($z = 2$ for Ca^{2+}) and moderated electronic restructuring, rather

than a simple reduction in electrochemical performance. Electrochemical measurements confirm these results: Ca-intercalated TiS_2 delivers a first-cycle capacity of 201 $mAh \cdot g^{-1}$, superior diffusion coefficients, and 96.3% rate retention with stable cycling. This work provides the first atomistic evidence that Ca^{2+} insertion facilitates ion transport while imparting structural resilience, offering a design framework for next-generation multivalent-ion batteries.

Keywords: Ca-ion batteries; structural stability; first-principles calculations; TiS_2 (titanium disulfide)

1. INTRODUCTION

Lithium-ion batteries (LIBs) have long served as the cornerstone of modern energy-storage technology for portable electronics and electric vehicles owing to their high energy density, long cycle life, and excellent reversibility [1–3]. However, the growing demand for batteries with higher energy density, coupled with the limited availability of lithium resources and ongoing safety concerns, has intensified the search for next-generation systems [4–7]. Among the alternatives, multivalent-ion batteries (MIBs) that utilize charge carriers such as Mg^{2+}, Ca^{2+}, Zn^{2+}, and Al^{3+} are receiving considerable attention. Because multivalent ions can transfer multiple electrons per ion, they can theoretically store more charge than conventional monovalent-ion systems [8,9].

Among MIBs, calcium-ion batteries (CIBs) are particularly promising. The standard reduction potential of Ca^{2+} (−2.87 V vs. SHE) is close to that of Li^{+} (−3.05 V), yet Ca^{2+} is a divalent charge carrier [10–14]. This combination of high operating voltage and divalent charge transport implies that CIBs can achieve energy densities comparable to—or even surpassing— those of LIBs [15,16]. Furthermore, calcium is naturally abundant, low cost, and environmentally benign, which enhances its potential for large-scale and sustainable energy-storage applications. Despite these advantages, the fundamental understanding of how Ca^{2+} interacts with host materials—particularly in terms of bonding, diffusion, and electronic structure—remains incomplete, hindering further progress in this field.

In pursuit of suitable electrode materials for CIBs, layered transition-metal dichalcogenides such as TiS_2, MoS_2, and WS_2 have emerged as attractive candidates owing to their two-dimensional frameworks that can accommodate large cations [17–19]. Among them,

TiS_2 is particularly notable for its narrow bandgap and wide interlayer spacing (0.57 nm), which is considerably larger than that of graphite (0.357 nm) [20–27]. These structural characteristics facilitate ion intercalation and diffusion, reduce energy barriers for insertion, and maintain lattice stability during cycling. As such, TiS_2 provides a well-defined model platform for exploring ion–host interactions in multivalent-ion systems.

In parallel, TiS_2 has also been actively investigated as a cathode material for lithium-ion batteries, where its layered structure enables rapid Li^+ transport through van der Waals gaps and reversible intercalation without severe lattice collapse. Recent studies have shown that Li^+ insertion in TiS_2 has been reported to exhibit different mechanistic features, including solid-solution-type behavior as well as phase-transition-related (two-phase) characteristics, depending on electrochemical conditions, accompanied by reversible Ti redox reactions and relatively fast reaction kinetics [28–30]. Spectroscopic and theoretical analyses further revealed that strong hybridization between Ti 3d and S 3p orbitals and the intrinsically high electronic conductivity of TiS_2 play key roles in governing Li^+ intercalation energetics [31,32]. At the same time, intrinsic limitations such as modest operating voltage and gradual structural or interfacial degradation during prolonged cycling have been reported in lithium-based TiS_2 systems [33,34]. However, these accumulated Li-ion studies establish TiS_2 as a well-characterized monovalent-ion host, providing a solid reference framework for extending investigations toward multivalent-ion intercalation.

Nevertheless, studies on Ca-ion intercalation in TiS_2 remain scarce, with only a few published to date. Tchitchekova et al. first demonstrated Ca^{2+} intercalation into TiS_2 at elevated temperatures using a $Ca(BF_4)_2$-based electrolyte [35]. Subsequently, our group

successfully inserted Ca ions at room temperature using a $Ca(CF_3SO_3)_2$-based electrolyte, demonstrating its practicality [36]. To further assess the system's applicability under broader electrochemical environments, the investigation was extended to aqueous high-concentration electrolytes [37]. While these studies verified the feasibility of Ca-ion storage, they offered limited insight into atomic-level processes such as ion migration, charge transfer, and structural evolution, which are essential to understanding and improving long-term performance. In this context, Li^+ intercalation in TiS_2 is intentionally employed in this work as a well-established monovalent reference system with extensively studied thermodynamic and kinetic characteristics. By directly comparing Li^+ and Ca^{2+} intercalation within an identical TiS_2 host lattice, this study aims to decouple the effects of ionic valence and charge compensation on adsorption energetics, diffusion barriers, and electronic-structure evolution. Such a comparative framework enables Ca^{2+}-specific behaviors to be interpreted against a clear physical baseline, thereby clarifying the unique challenges and opportunities associated with divalent-ion intercalation beyond what can be inferred from Ca-only investigations.

In this work, theoretical and experimental approaches are combined to investigate the structural, electronic, and kinetic behavior of Li^+ and Ca^{2+} intercalation in TiS_2. Density functional theory (DFT) and discrete variational Xα (DV-Xα) methods were employed to analyze diffusion barriers, bonding topology, and charge redistribution. The theoretical predictions were validated through galvanostatic cycling and cyclic voltammetry (CV) measurements, establishing direct correlations between atomic-scale interactions and electrochemical performance. This integrated framework not only bridges the gap between existing theoretical and experimental studies but also provides atomic-level design principles

for developing durable and high-performance CIBs.

2. METHODS

2.1. Cluster Model Setup for Intercalation Studies

To investigate the intercalation behavior of Li^+ and Ca^{2+} ions in TiS_2, a finite cluster model was constructed to approximate the local coordination geometry and electronic environment of bulk TiS_2. This cluster-based approach enables localized analysis of interfacial bonding, ion diffusion mechanisms, and structural perturbations during intercalation. The model comprises 26 Ti atoms and 48 S atoms, corresponding to a representative segment of the layered TiS_2 framework. To simulate ion-insertion conditions, 13 guest ions (Li^+ or Ca^{2+}) were introduced into the interlayer spacing, maintaining a stoichiometric ratio consistent with experimental intercalation levels. The charge state of the system was adjusted to reflect the formal oxidation states of the host and guest species, preserving overall charge neutrality. This configuration permits a direct comparison of Li and Ca intercalation under equivalent structural constraints and enables detailed evaluation of site-specific bonding and mobility.

2.2. Structural Optimization Using VASP

First-principles density functional theory (DFT) calculations were performed using the Vienna Ab Initio Simulation Package 5.4 (VASP) to optimize the atomic structures of $LiTiS_2$ and $CaTiS_2$. Structural relaxation accounted for volume changes and lattice distortions induced by ion intercalation, providing a reliable foundation for electronic structure analysis.

The exchange–correlation energy was treated using the generalized gradient approximation with the Perdew–Burke–Ernzerhof functional, striking a balance between computational efficiency and accuracy. A Monkhorst–Pack k-point mesh of 9 × 9 × 3 was employed with a 500 eV plane-wave cutoff, and convergence criteria were set to an energy difference below 10^{-5} eV and atomic forces below 0.01 eV·Å^{-1}. No explicit long-range dispersion (vdW) correction (e.g., DFT-D3 or vdW-DF) was applied in the present calculations. Although vdW interactions can contribute to interlayer binding in pristine layered materials, the optimized lattice parameters of pristine TiS_2 obtained under our computational settings agree well with reported experimental values (Section 3.1). In ion-intercalated TiS_2, the interlayer interaction arises from a combination of electrostatic, covalent, and dispersion contributions. Because the present study is intended to compare Li^+ and Ca^{2+} intercalation under identical settings, the calculated structures and electronic descriptors are interpreted primarily in terms of relative trends rather than quantitative interlayer binding energies. In this study, the electronic-structure analysis is primarily focused on charge-transfer-driven bonding evolution associated with guest-ion insertion, which has been widely adopted as an effective framework for understanding ion-intercalated layered materials in previous first-principles studies [38–40]. The fully relaxed geometries from VASP then served as input for DV-Xα calculations, ensuring consistency between structural and electronic analyses and enabling a comprehensive evaluation of ion-induced structural evolution for CIB performance.

2.3. Electronic State and Bonding Analysis using DV-Xα

To investigate the electronic structure and bonding characteristics of TiS_2, the DV-Xα

method was employed, a self-consistent molecular orbital (MO) approach based on local density approximation. This technique enables orbital-level analysis of bonding and charge distribution, offering atomic-scale insights into ion–host interactions and conductivity. Orbital overlap between guest ions (Li^+ or Ca^{2+}) and host atoms (S and Ti) was examined to assess bonding strength, hybridization, and implications for ionic mobility. Density of states (DOS), effective charges, and covalent electron populations were additionally calculated to characterize electronic states, charge transfer, and their influence on diffusion barriers. Bandgaps were estimated using the "lvlshm" command to link electronic excitation with charge transport. These results complement the DFT results, providing a comprehensive understanding of both ionic and electronic processes in TiS_2.

2.4. Band Structure and OCV Analysis using VASP

The electronic band structure and theoretical open-circuit voltage (OCV) of Li- and Ca-intercalated TiS_2 systems were calculated using first-principles DFT, as implemented in VASP. A plane-wave cutoff energy of 500 eV was employed, and the energy-convergence criterion for ionic relaxation was set to 0.05 $eV \cdot Å^{-1}$ to ensure numerical stability. Band structure calculations were conducted along high-symmetry paths in the Brillouin zone using the optimized unit cell geometries, enabling analysis of the electronic bandgap and carrier mobility.

All band-structure calculations for pristine, Li-intercalated, and Ca-intercalated TiS_2 were performed within the same PBE(GGA)+U framework using identical computational parameters, enabling direct comparison of electronic-structure changes induced by different

intercalating ions. Within this consistent computational setting, the calculated band structures are used to analyze relative features such as band dispersion, band-edge shifts, and band-gap evolution associated with ion intercalation [41–43]. In this context, the band-gap values are discussed as descriptors of electronic-structure evolution under a unified theoretical framework, providing insight into how Li^+ and Ca^{2+} intercalation differently modulate the electronic states of TiS_2

The OCV was computed using the total energies of the intercalated and pristine structures, based on the following expression [44,45]:

$$OCV = -\frac{[\{E(\mathrm{Li}_n\mathrm{TiS}_2 \; or \; \mathrm{Ca}_n\mathrm{TiS}_2) - E(\mathrm{Li}_m\mathrm{TiS}_2 \; or \; \mathrm{Ca}_m\mathrm{TiS}_2) - (n-m)E(\mathrm{Li}_{bulk} \text{ or } \mathrm{Ca}_{bulk})}{(n-m) \times \mathrm{z}}$$

where $E(\mathrm{Li}_n\mathrm{TiS}_2$ or $\mathrm{Ca}_n\mathrm{TiS}_2)$ and $E(\mathrm{Li}_m\mathrm{TiS}_2$ or $\mathrm{Ca}_m\mathrm{TiS}_2)$ represent the total energies of the intercalated and less-intercalated states, respectively, and $E(\mathrm{Li}_{bulk}$ or $\mathrm{Ca}_{bulk})$ is the reference energy per Li or Ca atom, obtained by calculating the total energy of the corresponding bulk metallic crystal and normalizing it by the number of metal atoms in the unit cell. Here, z denotes the valence charge of the intercalating ion ($z = 1$ for Li^+ and z = 2 for Ca^{2+}), reflecting the number of electrons transferred per inserted ion. As the total energies are expressed in eV per formula unit, the resulting value corresponds directly to the potential in volts; therefore, an explicit Faraday constant is not required. This formulation enables a direct and quantitative comparison of the electrochemical potentials of $LiTiS_2$ and $CaTiS_2$.

2.5. Adsorption and Diffusion Energy Calculations

The adsorption energy (E_{ads}) of Li^+ and Ca^{2+} ions on TiS_2 surfaces was calculated using a standard expression widely employed in surface science [46]:

$$E_{\text{ads}} = E_{\text{TiS}_2+\text{ion}} - E_{\text{TiS}_2} - E_{\text{guest ion (bulk)}}$$

where $E_{\text{TiS}_2+\text{ion}}$ is the total energy of the TiS_2 structure with an adsorbed Li^+ or Ca^{2+} ion, E_{TiS_2} is the total energy of the pristine TiS_2 surface, and $E_{\text{guest ion (bulk)}}$ refers to the energy of Li or Ca in the bulk metallic state; the more negative the E_{ads} value, the more thermodynamically stable the ion host interface.

The diffusion energy barrier (E_{diff}) was evaluated by determining the minimum energy path between adjacent adsorption sites using the nudged elastic band (NEB) method [47]:

$$E_{\text{diff}} = E_{\text{TS}} - E_{\text{initial}}$$

where E_{initial} represents the total energy of the initial adsorption state, and E_{TS} denotes the energy of the transition state corresponding to the highest energy point along the diffusion pathway. The transition state is defined as the first-order saddle point on the potential energy surface, at which the atomic configuration experiences a maximum in energy along the reaction coordinate but remains locally stable in all perpendicular directions. This state therefore represents the kinetic bottleneck that governs ion migration within the host lattice [48]. Accordingly, E_{diff} corresponds to the activation energy required for ion diffusion, and its magnitude directly determines the rate of ion transport. A lower E_{diff} value indicates reduced kinetic resistance, leading to more facile ion migration and enhanced rate capability in electrochemical systems [49–52].

2.6. Experimental Methods

2.6.1. Fabrication of TiS_2 Composite Electrodes

TiS_2 powder (Sigma-Aldrich, St. Louis, MO, USA), Super P conductive carbon

(TIMCAL, Bodio, Switzerland), and poly(vinylidene fluoride) (Mw ≈ 534,000; Alfa Aesar, Haverhill, MA, USA) were mixed in a weight ratio of 7:2:1. The mixture was dispersed in *N*-methyl-2-pyrrolidone (Junsei Chemical, Tokyo, Japan) to form a homogeneous slurry. The TiS_2 powder used in this study was obtained from a commercial supplier (Sigma-Aldrich) and was used as received. The layered TiS_2 phase has been extensively characterized in prior studies using X-ray diffraction and Raman spectroscopy, which report characteristic diffraction peaks and vibrational modes under ambient conditions [29,53,54]. Accordingly, we cite these prior structural reports for phase identification, while the present work focuses on electrochemical evaluation under moisture-controlled, nonaqueous conditions. This slurry was cast onto 18 μm thick copper foil (UACJ Corporation, Tokyo, Japan) using a doctor blade and dried in a vacuum oven (OV-11, Jeio Tech, Daejeon, Republic of Korea) at 80 °C for 12 h. The dried electrodes were punched into 15.95 mm discs and transferred into an Ar-filled glove box (SK-G1200, Three-Shine, Daejeon, Republic of Korea) with H_2O and O_2 levels maintained below 0.5 ppm.

2.6.2. Electrochemical Evaluation

CR2032-type coin cells (Welcos, Daejeon, Republic of Korea) were assembled in an Ar-filled glove box (SK-G1200, Three-Shine). The TiS_2 composite electrode served as the working electrode, while lithium metal foil (Honjo Metal, Osaka, Japan) was used as both the counter and reference electrodes. The use of Li metal as a pseudo-reference electrode is considered reasonable in Ca^{2+}-based systems, as Ca metal is potentially unstable and exhibits high interfacial impedance [55]. A microporous polypropylene membrane (Celgard 2400,

Celgard, Charlotte, NC, USA) was used as the separator. The electrolyte consisted of 0.1 mol dm^{-3} $Ca(TFSI)_2$ (99% purity, TCI, Tokyo, Japan) dissolved in a 1:1 (v/v) mixture of ethylene carbonate and dimethyl carbonate (battery grade, ENCHEM, Cheonan, Republic of Korea). Galvanostatic charge–discharge tests were performed using a battery cycler (WBCS 3000, WonATech, Seoul, Republic of Korea) within a voltage range of 1.5–3.0 V at room temperature. C-rate tests were performed sequentially at 0.1C, 1C, 3C, 5C, and 10C, followed by a return to 0.1C to evaluate rate capability. CV measurements were conducted at varying scan rates of 0.2, 0.5, 0.7, and 1.0 $mV \cdot s^{-1}$ to analyze the redox behavior and diffusion-controlled kinetics of Li^+ and Ca^{2+} intercalation in the TiS_2 host.

3. RESULTS

3.1. Structural Properties of $LiTiS_2$ and $CaTiS_2$

The lattice parameters of pristine TiS_2 and its Li- and Ca-intercalated derivatives were obtained from VASP-based structural optimization and are summarized in Figure 1. The initial lattice parameters were based on experimental data reported by Whittingham et al. [56], ensuring accurate structural modeling. In TiS_2 (Figure 1a), the lattice parameter *a*, representing the in-plane S–S distance, is 3.406 Å, while the interlayer spacing, *c*, is 5.699 Å. Both agree well with the experimental values. For $LiTiS_2$ (Figure 1b), *a* increases slightly to 3.408 Å and *c* to 6.142 Å, indicating minor expansion owing to Li-ion intercalation. By contrast, $CaTiS_2$ (Figure 1c) exhibits more substantial increases, with *a* and *c* reaching 3.642 and 6.507 Å, respectively. All structures were modeled with P-3m1 (164) symmetry, ensuring consistency.

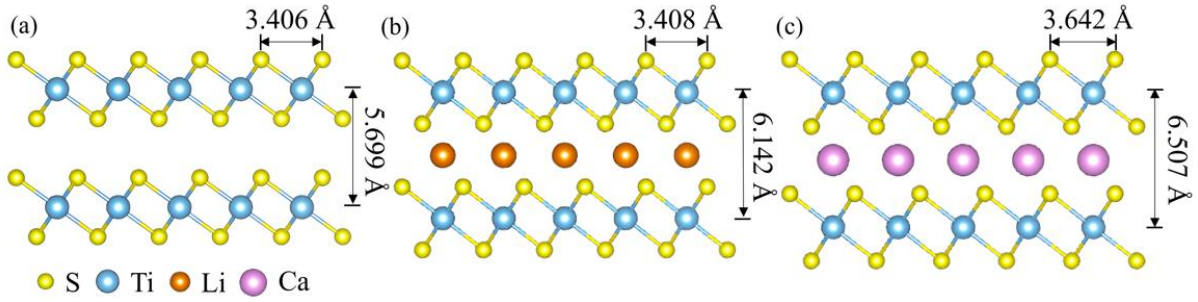

Figure 1. Structural schematics of (a) TiS_2, (b) $LiTiS_2$, and (c) $CaTiS_2$ in the (100) plane, highlighting the lattice parameters *a* and *c* with inserted guest ions.

Atomic-scale interactions in guest-ion-intercalated TiS_2 were examined using cluster models constructed for DV-Xα calculations. Based on these optimized structures, local bonding interactions and electron redistribution were further investigated. VASP provided structural optimization and total energy calculations, while DV-Xα offered complementary insights into localized bonding and hybridization. The clusters contained 1 mol of Li or Ca ions, with Li/Ca and Ti atoms aligned along the z-axis and S layers symmetrically positioned on either side. This setup simulated the layered bulk structure for comparative analysis (Figure 2). Owing to the larger ionic radius of Ca^{2+}, the Ca-intercalated cluster exhibits a more pronounced interlayer expansion than its Li-intercalated counterpart.

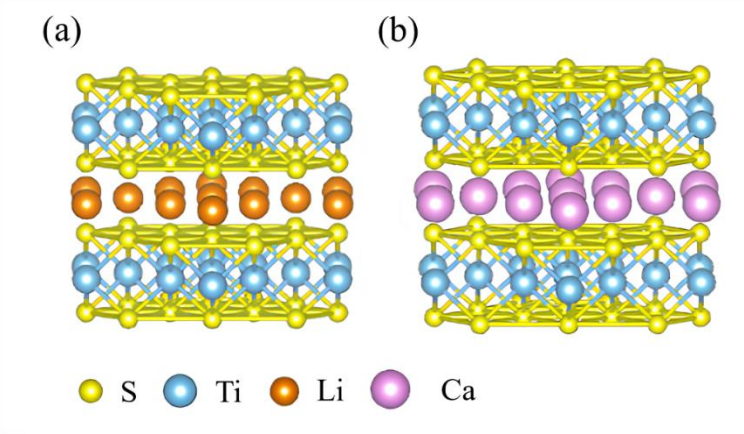

Figure 2. Cluster structures of (a) $LiTiS_2$ and (b) $CaTiS_2$ with guest ions situated between two layers in the (100) plane.

Following the bonding analysis, various cluster structures were considered, including XTi_2S_{12}, $X_7Ti_{14}S_{24}$, $X_7Ti_{14}S_{48}$, $X_{13}Ti_{14}S_{48}$, and $X_{13}Ti_{26}S_{48}$ (X = Li or Ca) (Figure S1). Among these, the $X_{13}Ti_{26}S_{48}$ structure was selected because it retains the 1:2 Ti:S ratio after ion insertion, maintaining charge balance for accurate modeling (Table S1). To evaluate electron distribution, the Madelung potential was applied to assign point charges: +1 for Li, +3 for Ti, and −2 for S in $LiTiS_2$; and +2 for Ca, +2 for Ti, and −2 for S in $CaTiS_2$. These values were introduced solely to construct the Madelung embedding potential and to define a consistent electrostatic reference for the DV-Xα population analysis. Accordingly, they should not be interpreted as representing macroscopic electrode charging or net charge accumulation during battery operation. To avoid confusion, explicit net-charge annotations for the finite clusters are omitted, and the DV-Xα results are discussed in terms of relative electron redistribution and bonding evolution within the Ti–S framework upon ion intercalation. This approach reflects the ionic nature of the layered materials and provides a physically consistent description of the local electrostatic environment in the embedded-cluster analysis.

3.2. Energy-Storage Properties and Overlap of Partial DOS

Following the structural analysis, the electronic properties were investigated to gain a deeper understanding of the influence of Li and Ca ions on the electronic behavior of TiS_2. The total/partial DOS and orbital-overlap characteristics were analyzed to provide a quantitative description of the intercalation-induced electronic-state evolution [57].

The DOS analysis was conducted by decomposing contributions from different orbital types, and bonding interactions were evaluated through orbital overlap density calculations, which measure the degree of electron sharing between atomic orbitals. A comparison of the total DOS reveals distinct electronic responses between $LiTiS_2$ and $CaTiS_2$, particularly near the Fermi level (Figure 3). The electron density at the Fermi level (E_F) for the $LiTiS_2$ cluster was measured to be only 0.88 eV^{-1}·unit $cell^{-1}$, in contrast to 1.96 eV^{-1}·unit $cell^{-1}$ for the $CaTiS_2$ cluster. This marked increase in DOS at E_F indicates that Ca intercalation modifies the electronic band structure and increases the density of states near E_F (Figure S2) [58,59].

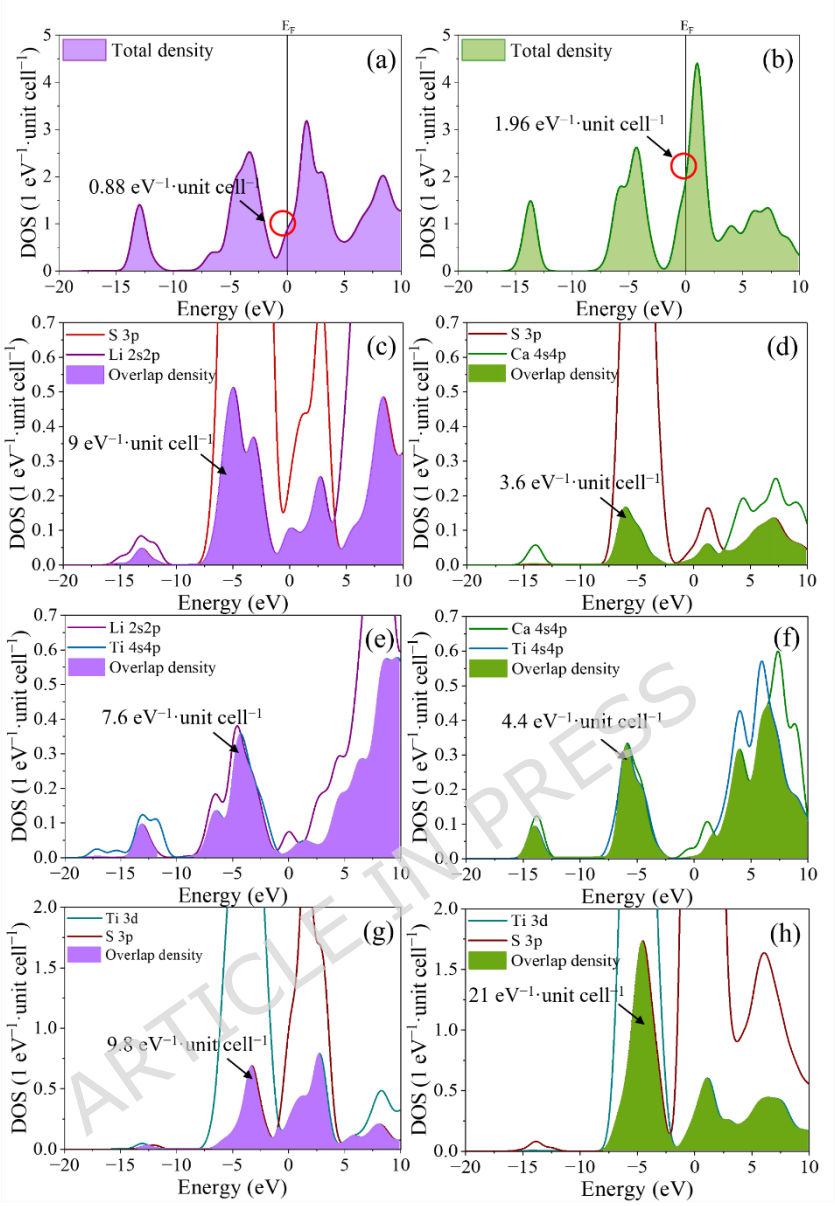

Figure 3. Comparison of DOS: (a) total DOS for the Li-intercalated structure $Li_{13}Ti_{26}S_{48}$; (b) total DOS for the Ca-intercalated structure $Ca_{13}Ti_{26}S_{48}$; partial DOS of the guest-ion sp and S 3p orbitals in (c) $Li_{13}Ti_{26}S_{48}$ and (d) $Ca_{13}Ti_{26}S_{48}$; partial DOS of the guest-ion sp and Ti 4s4p orbitals in (e) $Li_{13}Ti_{26}S_{48}$ and (f) $Ca_{13}Ti_{26}S_{48}$; and partial DOS of the S 3p and Ti 3d orbitals in (g) $Li_{13}Ti_{26}S_{48}$ and (h) $Ca_{13}Ti_{26}S_{48}$.

To further investigate the bonding interactions between the guest ions and the host material, the orbital overlap densities were calculated from the partial DOS. Guest-ion–S interactions were assessed using orbital-overlap densities, which indicate the extent of

electron sharing between the guest ion and sulfur. The overlap densities of 9 and 3.6 eV^{-1}·unit $cell^{-1}$ for $LiTiS_2$ and $CaTiS_2$, respectively, indicate weak bonding between Ca^{2+} and S atoms (Figure S3). The corresponding guest-ion–Ti overlap further differentiates the two intercalation chemistries, with Ca–Ti exhibiting a lower overlap than Li–Ti, where the overlap density for Ca–Ti interactions is 4.4 eV^{-1}·unit $cell^{-1}$, lower than that of Li–Ti (7.6 eV^{-1}·unit $cell^{-1}$). The orbital overlap density for Ti–S bonding is substantially higher in $CaTiS_2$ (21 eV^{-1}·unit $cell^{-1}$) than in $LiTiS_2$ (9.8 eV^{-1}·unit $cell^{-1}$). This lower orbital overlap reflects weaker ion–host binding strength (Figure S4), which reduces anchoring effects but may also compromise local structural rigidity, emphasizing the trade-off between ion mobility and framework stability [60].

3.3. Charge-Transfer Interactions in TiS_2 Interlayers

The influence of Li and Ca ions on charge-transfer interactions in TiS_2 interlayers was examined. To quantify the charge redistribution induced by intercalated ions during ion insertion (intercalation) within the interlayer galleries, the effective electron transfer from both guest ions and transition metals as well as sulfur atoms within the TiS_2 lattice was calculated. Here, the net charge derived from DV-Xα calculations refers to the effective charge associated with electron gain or loss due to partial and delocalized electron redistribution within the Ti–S framework, rather than a formal integer oxidation state. Because this descriptor is obtained from population analysis, it is used to discuss relative redistribution trends rather than to assign formal valence states. Accordingly, the sign and magnitude of the net charge indicate the direction and extent of electron accumulation or

depletion relative to the reference state, rather than formal redox transitions. Under the same definition, the reverse deintercalation process would yield an opposite sign.

The effective electron transfer from guest ions, transition metals, and sulfur atoms was quantified using the DV-Xα cluster method for both Li- and Ca-intercalated structures (Figure 4). Li ions contribute only +0.1 eV^{-1}·unit $cell^{-1}$, whereas Ca ions contribute +1.0 eV^{-1}·unit $cell^{-1}$, indicating stronger charge donation from Ca^{2+} during interlayer ion diffusion. Ti atoms also show comparable-magnitude net-charge responses in $CaTiS_2$ (+0.85 eV^{-1}·unit $cell^{-1}$) than in $LiTiS_2$ (+0.73 eV^{-1}·unit $cell^{-1}$). However, the Ti-related values should be interpreted as a population-analysis descriptor of partial and delocalized redistribution, not as a direct readout of formal oxidation states, because Ti–S bonding involves substantial covalent electron sharing. Notably, the DV-Xα analysis was performed for $Li_{13}Ti_{26}S_{48}$ and $Ca_{13}Ti_{26}S_{48}$ ($x \approx 0.5$) cluster models; therefore, even under an idealized ionic bookkeeping scheme, the average electron donation per Ti is fractional, and a one-to-one scaling of the Ti values with integer redox couples is not expected.

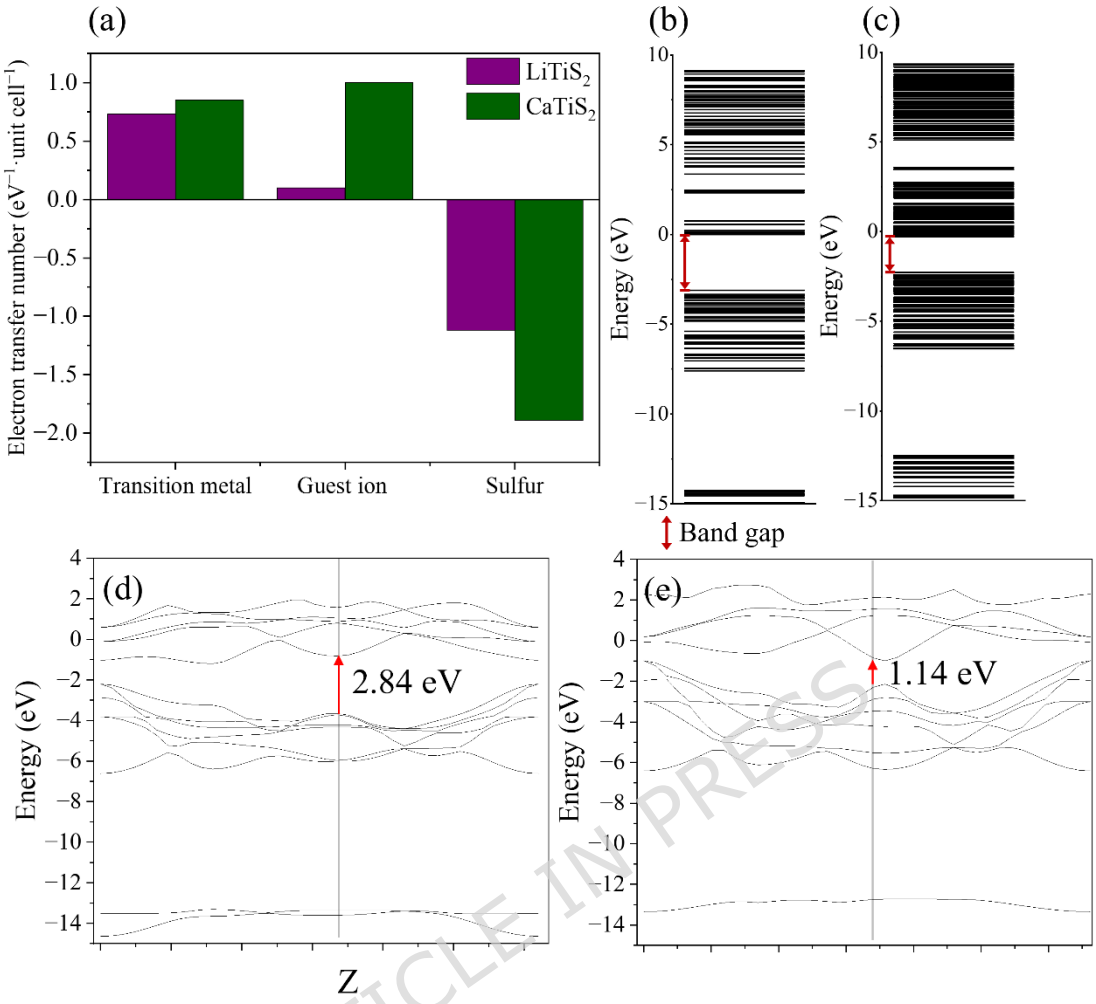

Figure 4. (a) Signed effective electron transfer (DV-Xα net charge) from guest ions, transition metals, and sulfur atoms in $Li_{13}Ti_{26}S_{48}$ and $Ca_{13}Ti_{26}S_{48}$; (b) MO diagram of $LiTiS_2$; (c) MO diagram of $CaTiS_2$; (d) band structure of bulk $LiTiS_2$; and (e) band structure of bulk $CaTiS_2$ (calculated using VASP and DV-Xα). In panel (a), positive and negative values indicate electron depletion and electron accumulation, respectively, within the adopted population-analysis definition.

When sulfur atoms are explicitly considered, they exhibit significant negative charge accumulation (−1.12 eV^{-1}·unit $cell^{-1}$ for $LiTiS_2$ and −1.89 eV^{-1}·unit $cell^{-1}$ for $CaTiS_2$), demonstrating that sulfur acts as an important charge-compensation site within the Ti–S framework. In $CaTiS_2$, the larger charge donation from Ca^{2+} is primarily reflected as increased electron accumulation on sulfur, rather than as a proportional change confined to Ti alone, whereas in $LiTiS_2$, the smaller charge donation from Li^+ results in a more modest

overall redistribution. Accordingly, even if an idealized formal-redox bookkeeping assigns different Ti redox couples to Li and Ca intercalation, the DV-Xα net-charge values on Ti can remain of comparable magnitude because the additional charge is redistributed over the covalent Ti–S network (not localized exclusively on Ti).

The molecular-orbital (MO) diagrams obtained from DV-Xα cluster calculations reveal distinct electronic reorganization in $LiTiS_2$ and $CaTiS_2$. The diagrams clearly show bandgap narrowing from 2.84 to 1.14 eV upon Ca insertion. The red square regions in Figures 4b and 4c mark the calculated MO gaps, highlighting the energy separation between the highest occupied and lowest unoccupied MOs. These electronic-structure changes reflect enhanced electronic delocalization induced by Ca^{2+} insertion during the charging process. Although the DV-Xα method is based on a finite cluster approximation, it reliably captures the relative evolution of electronic states associated with ion intercalation. Here, these values are interpreted as Kohn–Sham (model) gaps and are used as comparative descriptors of electronic-state evolution, rather than as quantitatively accurate quasiparticle band gaps. These electronic-structure changes reflect enhanced electronic delocalization induced by Ca^{2+} insertion during the charging process. Importantly, the bandgap values and their reduction trend are fully consistent with the bulk band-structure calculations performed using periodic DFT (VASP), as shown in Figures 4d and 4e. This result indicates that Ca^{2+} intercalation promotes enhanced electronic delocalization and strengthens host–guest charge coupling, as reflected in the overall evolution of the electronic structure. Similarly, in Figures 4d and 4e, the red arrows indicate the band-gap positions obtained from the bulk band-structure calculations using VASP, which are used to describe the relative separation between the

valence and conduction bands. The bulk calculations (Figures 4d and 4e) consistently reproduce the same qualitative trend, with $CaTiS_2$ exhibiting a substantially narrower band gap than $LiTiS_2$, thereby emphasizing the intercalation-induced band-gap narrowing rather than the absolute gap values (2.84 and 1.14 eV). The agreement between DV-Xα and periodic DFT calculations in capturing the relative band-gap evolution further demonstrates methodological consistency between localized and periodic electronic-structure analyses. These results are consistent with previous findings linking the band structure of TiS_2 to its charge-accommodation capability [61–64], confirming that Ca insertion enhances charge transfer and electronic conductivity.

3.4. Overlap Population Between Guest Ions and TiS_2 Host Material

The charge-transfer analysis reveals that the behavior of electrons in the $LiTiS_2$ and $CaTiS_2$ structures are distinct. To clarify the ion diffusion behavior and host structural integrity, orbital-level bonding interactions were examined using the overlap population (OP) method, which quantifies the extent to which bonding electrons occupy the valence band and antibonding electrons occupy the conduction band [66–68]. Representative OP diagrams for the $Li_{13}Ti_{26}S_{48}$ and $Ca_{13}Ti_{26}S_{48}$ clusters are shown in Figure 5, while results for other cluster sizes are provided in Figures S5 and S6.

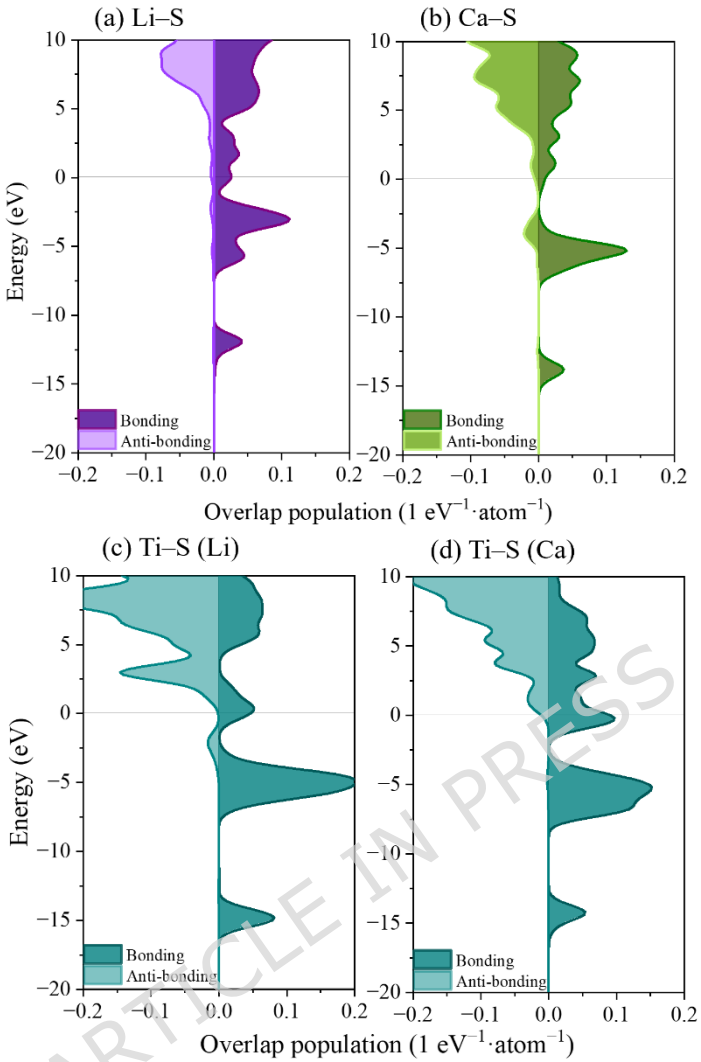

Figure 5. Overlap population diagrams for $Li_{13}Ti_{26}S_{48}$ and $Ca_{13}Ti_{26}S_{48}$: (a) Li–S bond; (b) Ca–S bond; (c) Ti–S bond in $Li_{13}Ti_{26}S_{48}$; and (d) Ti–S bond in $Ca_{13}Ti_{26}S_{48}$.

The bonding and antibonding electron densities for guest-ion–S and Ti–S interactions were quantified for both $LiTiS_2$ and $CaTiS_2$ clusters, as summarized in Table 1. For guest ion–S bonds, Li–S interactions exhibit a higher density of bonding electrons (0.183 $eV^{-1}·atom^{-1}$) and lower antibonding contribution (−0.0074 $eV^{-1}·atom^{-1}$) than Ca–S interactions (0.175 and −0.0193 $eV^{-1}·atom^{-1}$, respectively). This trend indicates that Ca–S bonds are weaker and more antibonding in nature, consistent with their higher ion mobility (Table S2). Conversely, for Ti–S bonds, $CaTiS_2$ shows a slightly higher bonding electron

density (0.346 vs. 0.338 $eV^{-1}\cdot atom^{-1}$) and lower antibonding contribution (−0.0042 vs. −0.0253 $eV^{-1}\cdot atom^{-1}$), indicating reinforced Ti–S covalency upon Ca insertion.

Table 1. Bonding and antibonding electron densities in $LiTiS_2$ and $CaTiS_2$ clusters.

Structure	Bonding	Bonding electrons ($eV^{-1}\cdot atom^{-1}$)	Anti-bonding electrons ($eV^{-1}\cdot atom^{-1}$)
$Li_{13}Ti_{26}S_{48}$	Li–S	0.183	−0.0074
	Ti–S	0.338	−0.0253
$Ca_{13}Ti_{26}S_{48}$	Ca–S	0.175	−0.0193
	Ti–S	0.346	−0.0042

Taken together, these bonding metrics quantitatively confirm that Ca intercalation weakens direct guest–host (Ca–S) anchoring while simultaneously strengthening host-framework (Ti–S) interactions. Such dual behavior provides a mechanistic basis for the observed balance between the enhanced ion diffusion and structural stability of $CaTiS_2$.

To quantify the bond strength, Figure 6 presents the integrated OP values. The effective covalent electron densities for Li–S and Ca–S bonds were 0.18 and 0.15 $eV^{-1}\cdot unit\ cell^{-1}$, respectively, confirming weaker bonding of Ca with S atoms. For Ti–S bonds, the integrated OP values were 0.31 for $LiTiS_2$ and 0.32 for $CaTiS_2$, indicating a slight strengthening of Ti–S interactions in the Ca-intercalated structure. Previous research has reported an effective covalent electron count of 0.38 $eV^{-1}\cdot unit\ cell^{-1}$ for Ti–S bonds in pristine TiS_2 [44]. Therefore, both $LiTiS_2$ and $CaTiS_2$ exhibited lower Ti–S covalency than pristine TiS_2, reflecting the redistribution of charge induced by guest-ion insertion (Table S3).

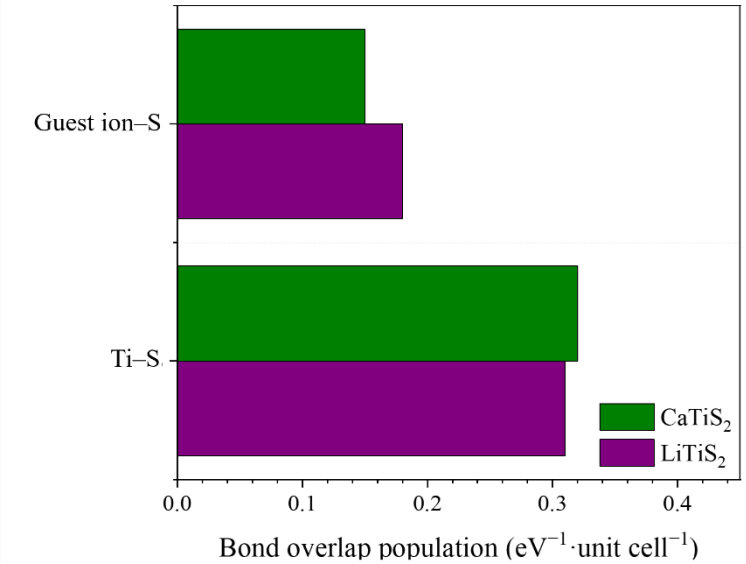

Figure 6. Effective covalent electron densities for guest ions, Ti, and S atoms in $Li_{13}Ti_{26}S_{48}$ and $Ca_{13}Ti_{26}S_{48}$.

3.5. Adsorption and Diffusion Characteristics of $LiTiS_2$ and $CaTiS_2$

Preferred ion-adsorption sites in the TiS_2 lattice were identified at the T (top of triangle) and H (center of hexagon) positions, corresponding to local energy minima for guest-ion accommodation (Figure 7a). Adsorption energies were evaluated for $LiTiS_2$ and $CaTiS_2$ in both the 1T and 2H polymorphs. $LiTiS_2$ exhibits −1.62 eV (T site) and −1.32 eV (H site), while $CaTiS_2$ shows more exothermic values of −2.89 eV (T site) and −1.43 eV (H site), indicating stronger binding for Ca and a clear preference for the T site in both systems (Figure 7b) [69,70]. It should be noted that the adsorption energy discussed here represents a static thermodynamic quantity describing the stability of an ion at an equilibrium site, whereas the diffusion barrier reflects a dynamic kinetic process governed by the activation energy along a predefined migration pathway [71–73]. Therefore, a more negative adsorption energy does not necessarily imply a higher diffusion barrier, as the two quantities are governed by different aspects of the potential energy surface.

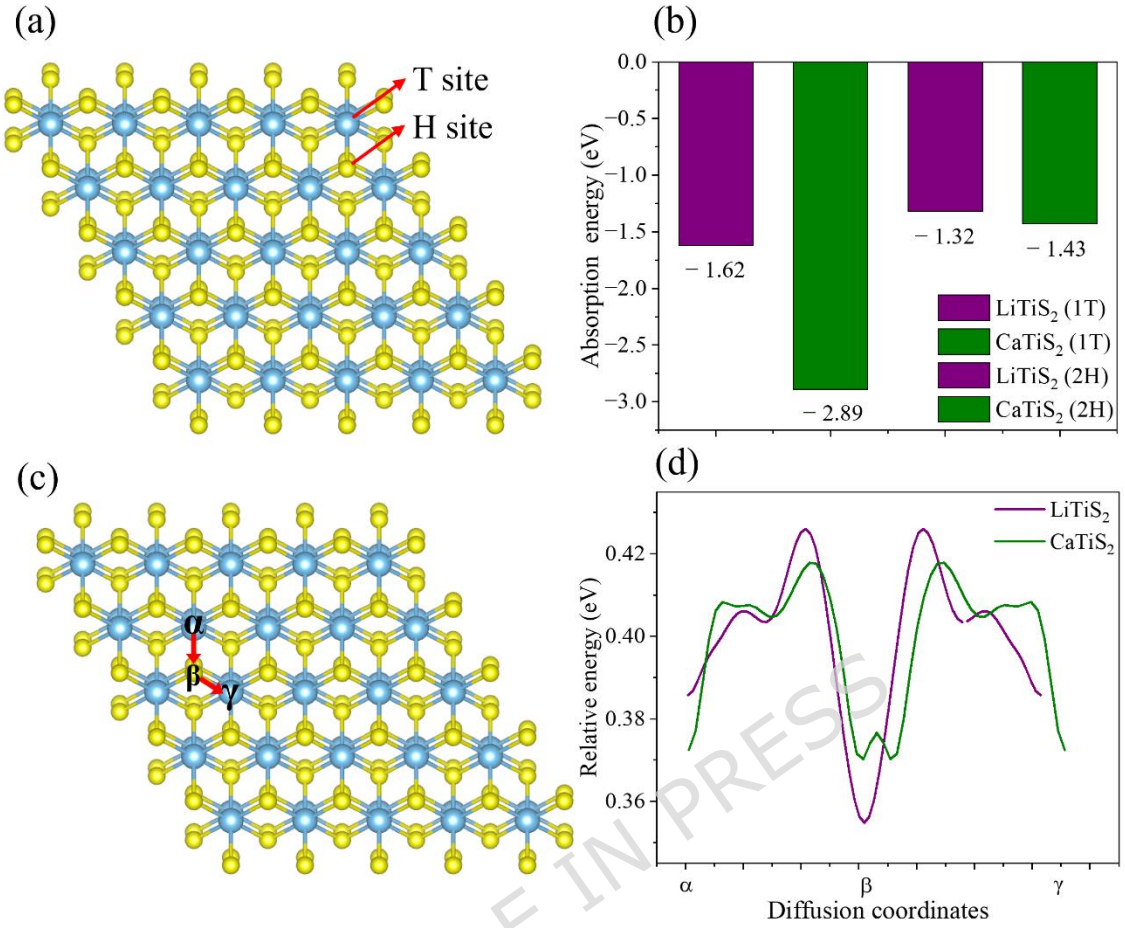

Figure 7. Adsorption and diffusion energy profiles of $LiTiS_2$ and $CaTiS_2$: (a) T and H sites within the TiS_2 structure; (b) adsorption energies of $LiTiS_2$ and $CaTiS_2$ for 1T and 2H phases; (c) diffusion pathways (α, β, γ) in TiS_2; and (d) relative diffusion energy profiles of $LiTiS_2$ and $CaTiS_2$ along α, β, and γ pathways.

To examine ion mobility within the TiS_2 lattice, three representative diffusion pathways were considered: α (T→H), β (T→T), and γ (H→H) (Figure 7c) [74,75]. $LiTiS_2$ exhibits a diffusion barrier of 0.07 eV along the α pathway, whereas $CaTiS_2$ shows a substantially lower value of 0.03 eV, corresponding to a reduction of approximately 0.04 eV. Along the β and γ pathways, $CaTiS_2$ also maintains lower barriers than $LiTiS_2$, confirming that Ca ions migrate more easily within the layered TiS_2 framework (Figure 7d).

3.6. Theoretical OCVs of $LiTiS_2$ and $CaTiS_2$

The bonding characteristics and lattice stability of $LiTiS_2$ and $CaTiS_2$ were used to evaluate their theoretical OCVs, which serves as a key descriptor of energy-storage efficiency and thermodynamic feasibility [76,77]. The OCV quantifies the maximum potential difference between electrodes under equilibrium and is thermodynamically linked to the Gibbs free energy change (ΔG) during ion intercalation.

Table 2. Theoretical OCVs for $LiTiS_2$ and $CaTiS_2$.

Structure	Open circuit voltage (V)
$LiTiS_2$	1.948
$CaTiS_2$	1.383

The calculated theoretical OCVs indicate that $LiTiS_2$ exhibits a higher value (1.948 V) than $CaTiS_2$ (1.383 V). Here, the reported OCV represents an average intercalation voltage between the selected reference states used in the OCV expression, and it does not constitute a composition-resolved voltage plateau. A full voltage profile (plateau diagram) would require total energies of intermediate Ca_xTiS_2 configurations and competing Ca/vacancy orderings, which is beyond the scope of the present dataset. Rather than simply indicating weaker insertion tendency, this difference implies that $LiTiS_2$ delivers a higher operating voltage and thus a higher energy density, while $CaTiS_2$ may operate in a lower voltage regime that can help suppress electrolyte decomposition and side reactions during cycling.

The lower OCV of $CaTiS_2$ is consistent with its more moderate electronic rearrangement and larger, yet structurally accommodated, lattice expansion upon ion insertion. These

characteristics imply that $CaTiS_2$ may experience reduced interfacial stress and potentially improved cycling stability, even though its energy output per charge is lower than that of $LiTiS_2$. Additionally, because Ca^{2+} transfers two electrons per ion, $CaTiS_2$ could achieve competitive charge storage despite operating in a lower voltage window.

Overall, these results indicate that $LiTiS_2$ offers higher energy output, while $CaTiS_2$ provides more favorable structural and interfacial behavior, reflecting a performance trade-off between energy density and long-term stability in Li^+ and Ca^{2+} intercalation systems.

3.7. Electrochemical Performance of TiS_2 Based on Capacity and Ion Transport

Galvanostatic charge–discharge profiles were analyzed to compare Li^+ and Ca^{2+} intercalation behavior in TiS_2. For Li intercalation, the first-cycle discharge capacity reached 134 $mAh \cdot g^{-1}$ (Figure 8a), while Ca intercalation achieved 201 $mAh \cdot g^{-1}$, confirming the greater charge-storage capability of $CaTiS_2$ (Figure 8b). In addition, $CaTiS_2$ exhibited a broader voltage plateau and reduced polarization compared to $LiTiS_2$, suggesting distinct reaction mechanisms between the two systems. These curve differences imply that, even under identical conditions using lithium metal as both counter and reference electrodes, the observed electrochemical behavior arises from genuine Ca^{2+} intercalation rather than Li^+ contamination.

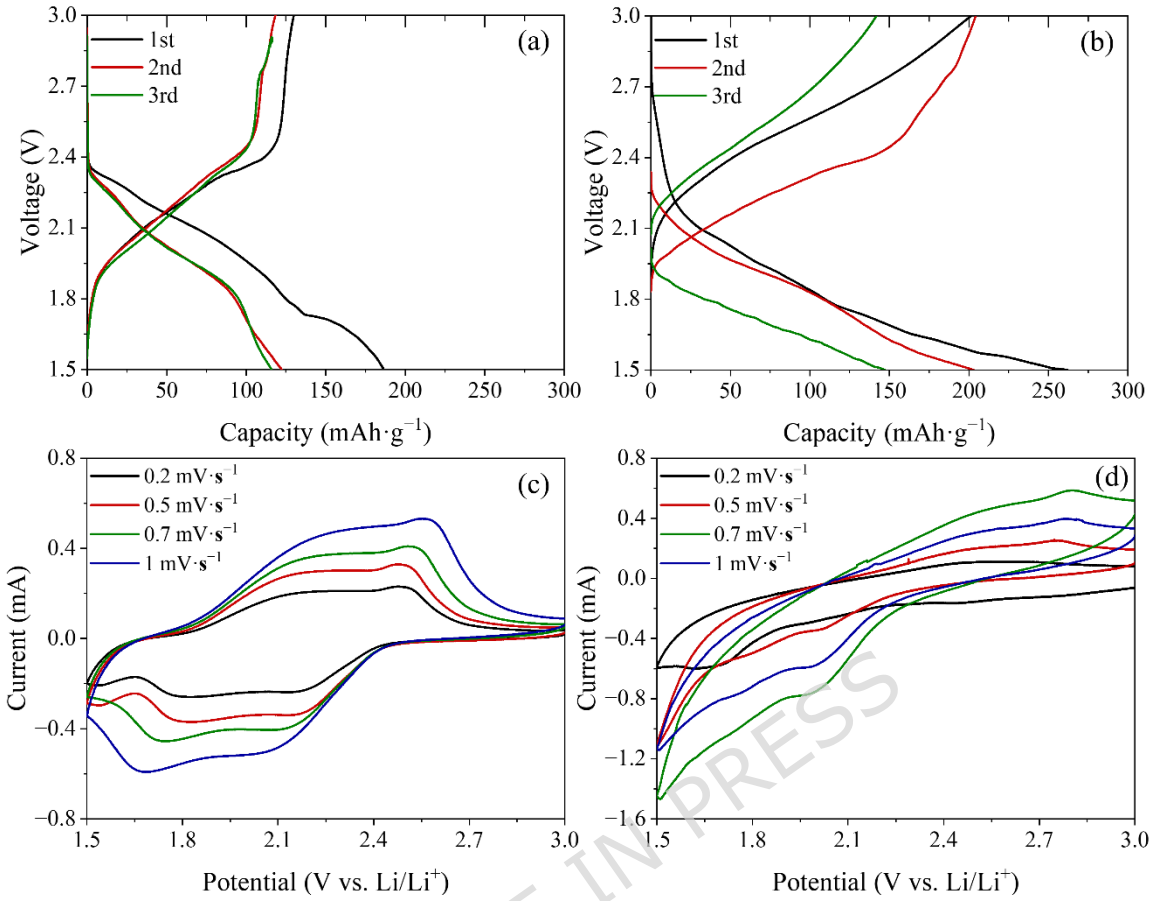

Figure 8. Electrochemical performance of TiS_2 electrodes upon Li^+ and Ca^{2+} intercalation. (a) Galvanostatic charge–discharge profiles of $LiTiS_2$ for the first three cycles, showing stable voltage plateaus near 1.8 and 2.3–2.5 V. (b) Charge–discharge profiles of $CaTiS_2$ for the first three cycles, exhibiting higher discharge capacity and distinct redox behavior with reduction ~2.0 V and oxidation near 2.8 V. (c) CV curves of $LiTiS_2$ at scan rates of 0.2–1.0 mV·s^{-1}, confirming diffusion-controlled Li^+ insertion/extraction. (d) CV curves of $CaTiS_2$ at varying scan rates, where broader and shifted peaks reflect enhanced Ca^{2+} transport kinetics within the TiS_2 host.

This interpretation is consistent with previous in situ XRD studies, which directly confirmed reversible Ca^{2+} insertion into the TiS_2 lattice without structural collapse [49]. In that report, characteristic diffraction peak shifts corresponding to (101) and (110) planes were observed during Ca^{2+} insertion and extraction, validating the intercalation mechanism. Taken together, the distinct voltage profiles obtained in this work and the structural evidence

reported earlier strongly support the successful insertion of Ca^{2+} ions into the TiS_2 host.

CV measurements also revealed distinct redox characteristics for Li and Ca insertion (Figures 8c and 8d). In $LiTiS_2$, a reduction peak corresponding to Li^+ insertion appeared near 1.8 V, and oxidation peaks related to Li^+ extraction were observed in the range of 2.3–2.5 V. In $CaTiS_2$, the reduction peak was shifted to ~2.0 V, while the oxidation peak arose at ~2.8 V. These differences highlight the distinct redox behavior of Li^+ and Ca^{2+} in the TiS_2 lattice. CV measurements were conducted at scan rates of 0.2, 0.5, 0.7, and 1.0 $mV \cdot s^{-1}$, and the corresponding increase in peak current with scan rate confirmed diffusion-controlled processes for both ions. The diffusion coefficients (D) of Li^+ and Ca^{2+} were calculated using the Randles–Sevcik equation [78]:

$$i_p = (2.69 \times 10^5) n^{3/2} A D^{1/2} C v^{1/2}$$

where i_p is the peak current (A), n is the number of electrons transferred, A is the electrode area (cm^2), D is the diffusion coefficient ($cm^2 \cdot s^{-1}$), C is the ion concentration ($mol \cdot cm^{-3}$), and v is the scan rate ($V \cdot s^{-1}$).

From the slopes of the i_p–$v^{1/2}$ plots, the diffusion coefficient of Li^+ was calculated to be 1.9×10^{-9} $cm^2 \cdot s^{-1}$, while that of Ca^{2+} was 3.1×10^{-9} $cm^2 \cdot s^{-1}$. The diffusion coefficients were determined by analyzing the anodic and cathodic peak currents at the respective redox potentials, confirming that Ca^{2+} exhibits faster ion transport than Li^+ in the TiS_2 host structure.

3.8. Impact of Li^+ and Ca^{2+} Intercalation on Rate Capability and Cycling Stability

The rate capability and long-term cycling performance of $LiTiS_2$ and $CaTiS_2$ electrodes

were systematically evaluated. In the rate capability test (Figure 9a), both electrodes exhibited reversible capacity recovery after returning to the initial current density. The capacity retention ratio after rate testing was 88.5% for $LiTiS_2$ and 96.3% for $CaTiS_2$, indicating that Ca intercalation leads to a higher rate capability than Li intercalation.

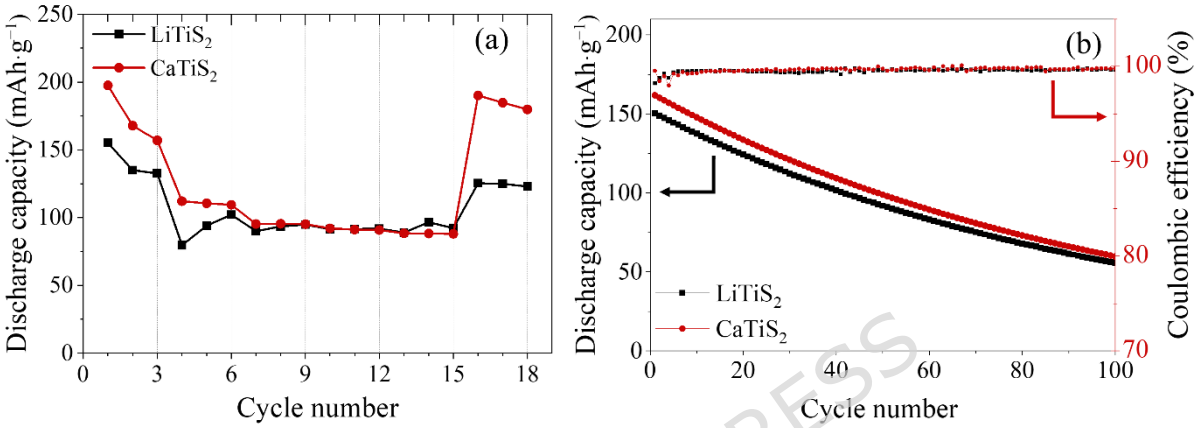

Figure 9. Cycling stability and rate capability of $LiTiS_2$ and $CaTiS_2$ electrodes. (a) Rate performance test, showing discharge capacities at varying current densities and subsequent recovery when the current returns to the initial condition. $CaTiS_2$ exhibits better capacity retention than $LiTiS_2$. (b) Long-term cycling performance over 100 cycles, where both electrodes show gradual capacity fading but maintain stable coulombic efficiency (~99% ± 1%). $CaTiS_2$ delivers slightly higher discharge capacities and comparable stability under identical conditions, confirming favorable structural tolerance to repeated intercalation.

The cycling performance over 100 cycles is shown in Figure 9b. After prolonged cycling, the capacity retention was 35.4% for $LiTiS_2$ and 36.6% for $CaTiS_2$, demonstrating that both systems possess comparable long-term stability under identical conditions. Despite the similar overall retention, $CaTiS_2$ consistently delivered slightly higher discharge capacities than $LiTiS_2$ during the cycling test. Coulombic efficiency remained stable at ~99% ± 1% throughout the cycles for both electrodes, confirming good reversibility of the intercalation process.

The gradual decrease in capacity observed during cycling can be attributed to structural degradation of the TiS_2 host, partial loss of the active material, and accumulation of resistive interfacial layers over repeated insertion/extraction. Nevertheless, the results confirm that Ca intercalation leads to a higher rate capability and cycling stability comparable to that of TiS_2 intercalated with Li.

4. DISCUSSION

The intercalation of multivalent cations into layered hosts has long been regarded as challenging owing to sluggish diffusion and structural instability. In particular, Ca^{2+} has often been considered unsuitable owing to its larger ionic radius and strong coulombic interactions. This study challenges these assumptions, demonstrating through a combined theoretical–experimental approach that TiS_2 can host Ca^{2+} ions both coherently and effectively while maintaining its layered integrity.

Theoretical analyses revealed three key features underlying this behavior. First, Ca^{2+} insertion resulted in a noticeable interlayer expansion that was greater than that of Li^+, which widened the diffusion channels but preserved crystallographic coherence through reinforced Ti–S bonding. This delicate balance between weaker guest anchoring and stronger host covalency created a previously unexplored insertion regime for divalent systems. Second, electronic structure calculations showed that Ca insertion markedly increased the DOS near the Fermi level and narrowed the bandgap, reflecting enhanced Ti orbital hybridization and suggesting improved electronic conductivity and redox activity. Third, orbital overlap analysis revealed that while Ca–host bonding relatively weakened, Ti–S covalency

strengthened, enabling facile ion mobility without structural breakdown. From a mechanistic perspective, the coexistence of strong adsorption and fast diffusion for Ca^{2+} originates from a decoupling between static ion stabilization and dynamic migration processes, as reported in previous theoretical studies [71—73]. While adsorption energy reflects the thermodynamic depth of local binding sites dominated by electrostatic interactions, ion diffusion is governed by the saddle-point energy along the migration pathway, which is strongly influenced by host covalency and electronic screening.

The experimental evidence supported these theoretical predictions. CV testing confirmed higher redox potentials for Ca insertion, while the kinetic analyses revealed unexpectedly fast ion transport consistent with the calculated low diffusion barriers. Long-term cycling stability measurements also demonstrated gradual rather than abrupt capacity decay, implying that the Ti–S framework remains mechanically resilient during repeated intercalation. Together, these results establish a new paradigm in divalent-ion intercalation: Ca^{2+} simultaneously weakens guest binding and strengthens host bonding, modifies band topology while expanding interlayers, and enhances charge transfer while minimizing diffusion barriers.

Beyond TiS_2, this work contributes a broader design principle for multivalent-ion hosts: maintaining weak guest–host binding to promote diffusion, ensuring strong host frameworks to resist degradation, enhancing DOS for improved conductivity, and controlling interlayer spacing to balance mobility and stability. The combined use of DV-Xα and DFT methodologies proved particularly powerful for correlating orbital-level interactions with experimentally measurable electrochemical behavior, underscoring the value of theory as

both predictive and explanatory. These findings establish Ca-intercalated TiS_2 as a robust prototype for advancing next-generation CIBs.

In the broader context of layered chalcogenide electrodes, the behavior observed in TiS_2 can be discussed alongside previous lithium-ion studies on MoS_2 and related materials. Prior work on MoS_2 has shown that Li^+ intercalation is often accompanied by pronounced interlayer expansion, electronic-structure modulation, and, in some cases, phase-transition-related structural rearrangements [79,80]. In comparison, the present results suggest that TiS_2 exhibits a more coherently balanced response during Ca^{2+} insertion, where interlayer expansion, electronic rehybridization, and host-framework stabilization occur without severe structural disruption. From this perspective, the present results point to the need and potential for extending integrated computational–electrochemical studies to a wider range of layered materials, enabling a more systematic correlation between electronic structure, bonding characteristics, and experimentally observed intercalation behavior in multivalent-ion systems.

5. CONCLUSIONS

This study demonstrates that Ca^{2+} intercalation into TiS_2 establishes a unique interplay between weakened guest anchoring, reinforced host covalency, and enhanced electronic activity. The cooperative effect of these factors enables rapid ion diffusion, efficient charge transfer, and high structural resilience, all of which overcome the traditional limitations of divalent-ion systems. By combining theoretical modeling and electrochemical validation, the work provides atomistic insight into how Ca^{2+} modifies the Ti–S lattice and electronic

framework, thereby redefining the criteria for viable multivalent-ion hosts.

Future research should focus on extending this strategy to other layered chalcogenides and exploring electrolyte compositions that further stabilize Ca^{2+} transport. Particular attention should be given to interfacial phenomena, where desolvation kinetics and charge-transfer barriers often dictate overall performance. Additionally, the integration of in situ characterization techniques with first-principles modeling will be essential to capture real-time structural dynamics during intercalation. By advancing this multiscale understanding, the design of durable, high-performance CIBs—and more broadly, next-generation multivalent systems—can be achieved with improved predictability and efficiency.

A quantitatively resolved thermodynamic assessment of Ca_xTiS_2 requires convex hull analysis across a broad Ca concentration range to evaluate phase stability/metastability and to test whether the electrochemical response is governed by solid-solution behavior or phase separation. Likewise, constructing a composition-resolved voltage profile and correlating voltage features with deintercalation-induced structural rearrangements would be necessary to quantitatively link structural evolution to cycling stability. Because these composition-dependent analyses require extensive additional sampling beyond the present dataset, they are identified here as key directions for future work

Funding: This work was supported by the Korea Institute of Energy Technology Evaluation and Planning (KETEP) and the Ministry of Trade, Industry & Energy (MOTIE) of the Republic of Korea (No. RS-2024-00394769). This research was supported by the Basic

Science Research Program through the National Research Foundation of Korea (NRF) funded by the Ministry of Education (NRF-2021R1I1A3060329). This study was supported by the Soonchunhyang University Research Fund.

Conflicts of Interest: The authors declare no conflict of interest.

REFERENCES

1. Kim, T., Song, W., Son, D.-Y., Ono, L. K. & Qi, Y. Lithium-ion batteries: outlook on present, future, and hybridized technologies. *J. Mater. Chem. A* **7**, 2942─2964 (2019).
2. Wakihara, M. Recent developments in lithium ion batteries. *Mater. Sci. Eng. R Rep.* **33**, 109─134 (2001).
3. Huang, B., Pan, Z., Su, X. & An, L. Recycling of lithium-ion batteries: Recent advances and perspectives. *J. Power Sources* **399**, 274–286 (2018).
4. Li, M. *et al.* Design strategies for nonaqueous multivalent-ion and monovalent-ion battery anodes. *Nat. Rev. Mater.* **5**, 276–294 (2020).
5. Liu, Z. *et al.* Ion migration and defect effect of electrode materials in multivalent-ion batteries. *Prog. Mater Sci.* **125**, 100911 (2022).
6. Huie, M. M., Bock, D. C., Takeuchi, E. S., Marschilok, A. C. & Takeuchi, K. J. Cathode materials for magnesium and magnesium-ion based batteries. *Coord. Chem. Rev.* **287**, 15–27 (2015).
7. Medina, A., Pérez-Vicente, C. & Alcántara, R. Advancing towards a practical magnesium ion battery. *Materials* **14**, 7488 (2021).
8. Huang, J., Xie, X., Liu, K., Liang, S. & Fang, G. Perspectives in Electrochemical In Situ Structural Reconstruction of Cathode Materials for Multivalent-Ion Storage. *Energy Environ. Mater.* **6**, e12309 (2023).
9. Taghavi-Kahagh, A., Roghani-Mamaqani, H. & Salami-Kalajahi, M. Powering the future: A comprehensive review on calcium-ion batteries. *J. Energy Chem.* **90**, 77─97

(2024).

10. Wu, Y. *et al.* Cathode materials for calcium-ion batteries: Current status and prospects. *Carbon Neutralization* **2**, 551─573 (2023).

11. Ji, B., He, H., Yao, W. & Tang, Y. Recent advances and perspectives on calcium-ion storage: key materials and devices. *Adv. Mater.* **33**, 2005501 (2021).

12. Maroni, F., Dongmo, S., Gauckler, C., Marinaro, M. & Wohlfahrt-Mehrens, M. Through the maze of multivalent-ion batteries: a critical review on the status of the research on cathode materials for Mg^{2+} and Ca^{2+} ions insertion. *Batter. Supercaps.* **4**, 1221─1251 (2021).

13. Deng, X. *et al.* Anode chemistry in calcium ion batteries: a review. *Energy Storage Mater.* **53**, 467─481 (2022).

14. Tojo, T., Tawa, H., Oshida, N., Inada, R. & Sakurai, Y. Electrochemical characterization of a layered α-MoO_3 as a new cathode material for calcium ion batteries. *J. Electroanal. Chem.* **825**, 51─56 (2018).

15. Tinker, H. R., Howard, C. A., Zhou, M. & Xu, Y. Exploring anodes for calcium-ion batteries. *Mater. Adv.* **4**, 2028─2041 (2023).

16. Yao, Z., Hegde, V. I., Aspuru-Guzik, A. & Wolverton, C. Discovery of calcium-metal alloy anodes for reversible Ca-ion batteries. *Adv. Energy Mater.* **9**, 1802994 (2019).

17. Chen, S.-M. Preparation, characterization, and electrocatalytic oxidation properties of iron, cobalt, nickel, and indium hexacyanoferrate. *J. Electroanal. Chem.* **521**, 29─52 (2002).

18. Wang, D. *et al.* Plating and stripping calcium in an organic electrolyte. *Nat. mater.* **17**,

16–20 (2018).

19. Adil, M. *et al.* Practical aqueous calcium-ion battery full-cells for future stationary storage. *ACS Appl. Mater. Interfaces* **12**, 11489–11503 (2020).

20. Lee, C. & Jeong, S.-K. A novel superconcentrated aqueous electrolyte to improve the electrochemical performance of calcium-ion batteries. *Chem. Lett.* **45**, 1447–1449 (2016).

21. Jin Li, Chengjun Han, Xuewu Ou & Yongbing Tang. Concentrated Electrolyte for High-Performance Ca-Ion Battery Based on Organic Anode and Graphite Cathode. *Angew. Chem. Int.* **14**, e202116668 (2022).

22. Dompablo, M. E. A.-d. *et al.* A joint computational and experimental evaluation of $CaMn_2O_4$ polymorphs as cathode materials for Ca ion batteries. *Chem. Mater.* **28**, 6886–6893 (2016).

23. Whittingham, M. S. Lithium batteries and cathode materials. *Chem. Rev.* **104**, 4271–4302 (2004).

24. Verrelli, R. *et al.* Steps towards the use of TiS_2 electrodes in Ca batteries. *J. Electrochem. Soc.* **167**, 070532 (2020).

25. Chhowalla, M. *et al.* The chemistry of two-dimensional layered transition metal dichalcogenide nanosheets. *Nat. Chem.* **5**, 263–275 (2013).

26. Tian, R. *et al.* Adsorption and diffusion of alkali metals (Li, Na, and K) on heteroatom-doped monolayer titanium disulfide. *Dalton Trans.* **50**, 7065–7077 (2021).

27. Safaeipour, S., Kalantarian, M. M., Shabani, M. O. & Faeghinia, A. Investigation on

TiS_2 electrode material for intercalation batteries, namely Li, Na, Mg, Al, K, Ca, and Zn-ion cells: A DFT study. *Results Chem.* **7**, 101347 (2024).

28. Ma, L. *et al.* Hybrid cathode architectures for lithium batteries based on TiS_2 and sulfur. *J. Mater. Chem. A* **3**, 19857–19866 (2015).

29. Oh, D. Y. *et al.* All-solid-state lithium-ion batteries with TiS_2 nanosheets and sulphide solid electrolytes. *J. Mater. Chem. A* **4**, 10329–10335 (2016).

30. Kim, J. Y. *et al.* Revisiting TiS_2 as a diffusion-dependent cathode with promising energy density for all-solid-state lithium secondary batteries. *Energy Storage Mater.* **41**, 289–296 (2021).

31. Jiang, Y. *et al.* Advances in TiS_2 for energy storage, electronic devices, and catalysis: A review. *Prog. Nat. Sci. Mater. Int* **33**, 133–150 (2023).

32. Hu, P., Wang, B., Xiao, D. & Aifantis, K. Capturing the differences between lithiation and sodiation of nanostructured TiS_2 electrodes. *Nano Energy* **63**, 103820 (2019).

33. Miranda, J., Franklin, G., Mathis, T. S., Taberna, P.-L. & Simon, P. Unraveling the two-phase lithiation process in TiS_2 by using the combination of operando EQCM and Electrochemical Dilatometry techniques. *Energy Storage Mater.* **65**, 103105 (2024).

34. Zhang, L. *et al.* Tracking the Chemical and Structural Evolution of the TiS_2 Electrode in the Lithium-Ion Cell Using Operando X-ray Absorption Spectroscopy. *Nano Lett.* **18**, 4506–4515 (2018).

35. Tchitchekova, D. S. *et al.* Electrochemical intercalation of calcium and magnesium in TiS_2: fundamental studies related to multivalent battery applications. *Chem. Mater.* **30**, 847−856 (2018).

36. Lee, C. *et al.* Electrochemical intercalation of Ca^{2+} ions into TiS_2 in organic electrolytes at room temperature. *Electrochem. Commun.* **98**, 115─118 (2019).

37. Seong, S. *et al.* Application of TiS_2 as an active material for aqueous calcium-ion batteries: electrochemical calcium intercalation into TiS_2 from aqueous solutions. *Batteries* **9**, 500 (2023).

38. Wan, L. F., Incorvati, J. T., Poeppelmeier, K. R. & Prendergast, D. Building a Fast Lane for Mg Diffusion in α-MoO_3 by Fluorine Doping. *Chem. Mater.* **28**, 6900–6908 (2016).

39. Wiedemann, D. *et al.* Lithium Diffusion Pathways in 3R-Li_xTiS_2: A Combined Neutron Diffraction and Computational Study. *J. Phys. Chem. C* **119**, 11370–11381 (2015).

40. Rong, Z. *et al.* Materials Design Rules for Multivalent Ion Mobility in Intercalation Structures. *Chem. Mater.* **27**, 6016–6021 (2015).

41. Long, O. Y., Sai Gautam, G. & Carter, E. A. Assessing cathode property prediction via exchange-correlation functionals with and without long-range dispersion corrections. *Phys. Chem. Chem. Phys.* **23**, 24726–24737 (2021).

42. Isaacs, E. B., Patel, S. & Wolverton, C. Prediction of Li intercalation voltages in rechargeable battery cathode materials: Effects of exchange-correlation functional, van der Waals interactions, and Hubbard U. *Phys. Rev. Mater.* **4**, 065405 (2020).

43. Alshomar, S., Mansouri, M. & Azhary, A. First principles study on the effects of Li deintercalation on the structural properties of a novel mixed transition metal cathode material $LiNi_{0.75}Mn_{0.125}Fe_{0.125}PO_4$ and investigation of its electric properties. *Ceram.*

Int. **50**, 26402–26409 (2024).

44. Kim, Y.-S., Mizuno, M., Tanaka, I. & Adachi, H. Electronic structure and chemical bonding of TiS_2 by cluster calculation. *Mater. Trans., JIM* **39**, 709─713 (1998).

45. Park, H., Bartel, C. J., Ceder, G. & Zapol, P. Layered Transition Metal Oxides as Ca Intercalation Cathodes: A Systematic First-Principles Evaluation. *Adv. Energy Mater.* **11**, 2101698 (2021).

46. He, Q., Yu, B., Li, Z. & Zhao, Y. Density Functional Theory for Battery Materials. *Energy Environ. Mater.* **2**, 264─279 (2019).

47. Park, J. & Afrinish Fatima, S. A DFT study of TiC_3 as anode material for Li-ion batteries. *Appl. Surf. Sci.* **638**, 158024 (2023).

48. Henkelman, G. & Jónsson, H. Improved tangent estimate in the nudged elastic band method for finding minimum energy paths and saddle points. *J. Chem. Phys.* **113**, 9978–9985 (2000).

49. Xu, G., Zhong, K., Zhang, J.-M. & Huang, Z. First-principles investigation of the electronic and Li-ion diffusion properties of $LiFePO_4$ by sulfur surface modification. *J. Appl. Phys.* **116** (2014).

50. Liu, M. *et al.* Spinel compounds as multivalent battery cathodes: a systematic evaluation based on ab initio calculations. *Energy Environ. Sci.* **8**, 964─974 (2015).

51. Kim, D.-w. *et al.* Full picture discovery for mixed-fluorine anion effects on high-voltage spinel lithium nickel manganese oxide cathodes. *NPG Asia Mater.* **9**, e398─e398 (2017).

52. Ma, X., Kang, B. & Ceder, G. High Rate Micron-Sized Ordered $LiNi_{0.5}Mn_{1.5}O_4$. *J.*

Electrochem. Soc. **157**, A925 (2010).

53. Sharma, S., Singh, S., Singh, R. C. & Sharma, S. Structural transformation and room temperature ammonia sensing properties of TiS_2 nanostructures. *SN appl. sci.* **2**, 887 (2020).

54. Sherrell, P. C. *et al.* Thickness-Dependent Characterization of Chemically Exfoliated TiS_2 Nanosheets. *ACS Omega* **3**, 8655–8662 (2018).

55. Tchitchekova, D. *et al.* On the reliability of half-cell tests for monovalent (Li^+, Na^+) and divalent (Mg^{2+}, Ca^{2+}) cation based batteries. *J. Electrochem. Soc.* **164**, A1384 (2017).

56. Whittingham, M. S. Electrical energy storage and intercalation chemistry. *Science* **192**, 1126─1127 (1976).

57. Zhou, C., Yang, W., Wu, Y., Lin, W. & Zhu, H. Theoretical study of the interaction of electron donor and acceptor molecules with monolayer WS_2. *J. Phys. D: Appl. Phys.* **48**, 285303 (2015).

58. Wang, W. *et al.* First-principles investigations of vanadium disulfide for lithium and sodium ion battery applications. *RSC Adv.* **6**, 54874─54879 (2016).

59. Li, S., Liu, J. & Liu, B. First principles study of nanostructured TiS_2 electrodes for Na and Mg ion storage. *J. Power Sources* **320**, 322─331 (2016).

60. Kim, Y.-S., Koyama, Y., Tanaka, I. & Adachi, H. Chemical bondings around intercalated Li atoms in $LiTiX_2$ (X= S, Se, and Te). *J. Appl. Phys.* **37**, 6440 (1998).

61. Rinkel, B. L., Hall, D. S., Temprano, I. & Grey, C. P. Electrolyte oxidation pathways in lithium-ion batteries. *J. Am. Chem. Soc.* **142**, 15058─15074 (2020).

62. Zheng, J., Ren, Z., Guo, P., Fang, L. & Fan, J. Diffusion of Li^+ ion on graphene: A DFT study. *Appl. Surf. Sci.* **258**, 1651–1655 (2011).

63. Er, D., Li, J., Naguib, M., Gogotsi, Y. & Shenoy, V. B. Ti_3C_2 MXene as a high capacity electrode material for metal (Li, Na, K, Ca) ion batteries. *ACS Appl. Mater. Interfaces* **6**, 11173–11179 (2014).

64. Mishra, S. & Ceder, G. Structural stability of lithium manganese oxides. *Phys. Rev. B* **59**, 6120 (1999).

65. Marseglia, E. Transition metal dichalcogenides and their intercalates. *Int. Rev. Phys. Chem.* **3**, 177–216 (1983).

66. Segall, M., Shah, R., Pickard, C. J. & Payne, M. Population analysis of plane-wave electronic structure calculations of bulk materials. *Phys. Rev. B* **54**, 16317 (1996).

67. Mayer, I. & Salvador, P. Overlap populations, bond orders and valences for 'fuzzy'atoms. *Chem. Phys. Lett.* **383**, 368–375 (2004).

68. Mizoguchi, T. Overlap population diagram for ELNES and XANES: peak assignment and interpretation. *J. Phys.: Condens. Matter* **21**, 104215 (2009).

69. Chaoui, K. *et al.* MoS_2 and WSe_2 monolayers as anode materials for future Li, Na, and K ion batteries under electric field effect. *J. Energy Storage* **109**, 115110 (2025).

70. Wang, P.-Y., Yeh, C.-C., Chiu, M.-J. & Chiu, C.-c. A comparative study on the linear scaling relations for the diffusion of S-vacancies on MoS_2 and WS_2. *Phys. Chem. Chem. Phys.* **26**, 5070–5080 (2024).

71. Tu, K., Li, F. & Chen, Z. Enhanced lithium adsorption/diffusion and improved Li capacity on SnS2 nanoribbons: A computational investigation. *J. Mater. Res.* **31**, 878–

885 (2016).

72. Jin, M., Yu, L. C., Shi, W. M., Deng, J. G. & Zhang, Y. N. Enhanced Absorption and Diffusion Properties of Lithium on B,N,V(C)-decorated Graphene. *Sci Rep* **6**, 37911 (2016).

73. Mukherjee, S., Banwait, A., Grixti, S., Koratkar, N. & Singh, C. V. Adsorption and Diffusion of Lithium and Sodium on Defective Rhenium Disulfide: A First Principles Study. *Appl. Mater. Interfaces* **10**, 5373–5384 (2018).

74. Zhao, S. *et al.* The effect of MoS_2 modified with transition metal (Fe, Co, Ni, Cu) on H_2O adsorption: A first principle study. *Micro Nanostructures* **197**, 208021 (2025).

75. Qi, J. *et al.* First-principles investigation of Boron-doped graphene/MoS_2 heterostructure as a potential anode material for Mg-ion battery. *Colloids and Surf. A: Physicochem. Eng. Asp.* **683**, 132998 (2024).

76. Pattipati, B., Balasingam, B., Avvari, G. V., Pattipati, K. R. & Bar-Shalom, Y. Open circuit voltage characterization of lithium-ion batteries. *J. Power Sources* **269**, 317─333 (2014).

77. Lee, S., Kim, J., Lee, J. & Cho, B. H. State-of-charge and capacity estimation of lithium-ion battery using a new open-circuit voltage versus state-of-charge. *J. Power Sources* **185**, 1367─1373 (2008).

78. Fleischmann, S., Shao, H., Taberna, P.-L., Rozier, P. & Simon, P. Electrochemically Induced Deformation Determines the Rate of Lithium Intercalation in Bulk TiS_2. *ACS Energy Lett.* **6**, 4173─4178 (2021).

79. Stephenson, T., Li, Z., Olsen, B. & Mitlin, D. Lithium ion battery applications of

molybdenum disulfide (MoS_2) nanocomposites. *Energy Environ. Sci.* **7**, 209–231 (2014).

80. Lu, X.-W. *et al.* Phase-engineered 1T′/2H-MoS_2 heterophase junctions for high-performance aqueous zinc-ion batteries. *Nanoscale* (2026).

Tables

Table 1. Bonding and antibonding electron numbers in $LiTiS_2$ and $CaTiS_2$ clusters.

Table 2. Theoretical OCVs for $LiTiS_2$ and $CaTiS_2$.

Figure legends

Fig. 1 Structural schematics of (a) TiS_2, (b) $LiTiS_2$, and (c) $CaTiS_2$ in the (100) plane, highlighting the lattice parameter a and c with inserted guest ions.

Fig. 2 Cluster structures of (a) $LiTiS_2$ and (b) $CaTiS_2$ with guest ions situated between two layers in the (100) plane.

Fig. 3 Comparison of the DOS: (a) total DOS for the Li-intercalated structure $Li_{13}Ti_{26}S_{48}$; (b) total DOS for the Ca-intercalated structure $Ca_{13}Ti_{26}S_{48}$; partial DOS of the guest ion sp and S 3p orbitals in (c) $Li_{13}Ti_{26}S_{48}$ and (d) $Ca_{13}Ti_{26}S_{48}$; partial DOS of the guest ion sp and Ti 4s4p orbitals in (e) $Li_{13}Ti_{26}S_{48}$ and (f) $Ca_{13}Ti_{26}S_{48}$; partial DOS of the S 3p and Ti 3d orbitals in (g) $Li_{13}Ti_{26}S_{48}$ and (h) $Ca_{13}Ti_{26}S_{48}$.

Fig. 4 (a) Signed effective electron transfer (DV-Xα net charge) from guest ions, transition metals, and sulfur atoms in $Li_{13}Ti_{26}S_{48}$ and $Ca_{13}Ti_{26}S_{48}$; (b) MO diagram of $LiTiS_2$; (c) MO diagram of $CaTiS_2$; (d) band structure of bulk $LiTiS_2$; and (e) band structure of bulk $CaTiS_2$ (calculated using VASP and DV-Xα). In panel (a), positive and negative values indicate electron depletion and electron accumulation, respectively, within the adopted population-analysis definition.

Fig. 5 Overlap population diagrams for $Li_{13}Ti_{26}S_{48}$ and $Ca_{13}Ti_{26}S_{48}$: (a) Li–S bond; (b) Ca–S

bond; (c) Ti–S bond in $Li_{13}Ti_{26}S_{48}$; (d) Ti–S bond in $Ca_{13}Ti_{26}S_{48}$.

Fig. 6 Effective covalent electron numbers for guest ions, Ti, and S atoms in $Li_{13}Ti_{26}S_{48}$ and $Ca_{13}Ti_{26}S_{48}$.

Fig. 7 Adsorption and diffusion energy profiles of $LiTiS_2$ and $CaTiS_2$: (a) T and H sites within the TiS_2 structure; (b) adsorption energies of $LiTiS_2$ and $CaTiS_2$ for 1T and 2H phases; (c) diffusion pathways (α, β, γ) in TiS_2; (d) relative diffusion energy profiles of $LiTiS_2$ and $CaTiS_2$ along α, β, and γ pathways.

Fig. 8 Electrochemical performance of TiS_2 electrodes upon Li^+ and Ca^{2+} intercalation. (a) Galvanostatic charge–discharge profiles of $LiTiS_2$ for the first three cycles, showing stable voltage plateaus near 1.8 and 2.3–2.5 V. (b) Charge–discharge profiles of $CaTiS_2$ for the first three cycles, exhibiting higher discharge capacity and distinct redox behavior with reduction around 2.0 V and oxidation near 2.8 V. (c) Cyclic voltammetry curves of $LiTiS_2$ at scan rates of 0.2–1.0 $mV \cdot s^{-1}$, confirming diffusion-controlled Li^+ insertion/extraction. (d) CV curves of $CaTiS_2$ at varying scan rates, where broader and shifted peaks reflect enhanced Ca^{2+} transport kinetics within the TiS_2 host.

Fig. 9 Cycling stability and rate capability of $LiTiS_2$ and $CaTiS_2$ electrodes. (a) Rate performance test, showing discharge capacities at various current densities and subsequent recovery when the current returns to the initial condition. $CaTiS_2$ exhibits superior capacity

retention compared with $LiTiS_2$. (b) Long-term cycling performance over 100 cycles, where both electrodes show gradual capacity fading but maintain stable Coulombic efficiency (~99 ± 1%). $CaTiS_2$ delivers slightly higher discharge capacities and comparable stability under identical conditions, confirming favorable structural tolerance to repeated intercalation.